Understanding the surface generation mechanism during micro-scratching of Ti-6Al-4V

Ashwani Pratap[1], Vishwas Divse[1], Saurav Goel[2,3,4] and Suhas S Joshi[1*]

[1] *Mechanical Engineering Department, Indian Institute of Technology Bombay, Powai, 400076, India*

[2] *London South Bank University, 103 Borough Road, London SE1 0AA, UK*

[3] *Department of Mechanical Engineering, Indian Institute of Technology Guwahati, Guwahati, 781039, India*

[4] *University of Petroleum and Energy Studies, Dehradun, 248007, India*

[*] *Corresponding author: ssjoshi@iitb.ac.in*

Abstract

A lot of grinding research in the past has been emulated using single grit scratching. This limits studying surface generation mechanism due to overlapping scratches inherent to the grinding process. It not only affects the surface generation mechanism, but also limits studying elastic recovery which has a significant effect on the final form and topography including the roughness generated after grinding. Taking Ti-6Al-4V as a testbed, this investigation was directed on comparing single scratches with adjacent scratches, which are often referred to as double scratches in literature. During the experiments, the effect of scratch speed, infeed angle and the scratch separation distance on the material removal mechanism in terms of cutting forces, material pile-up area ratio (PA), groove depth, material removal area (MRA) and sub-surface deformation were investigated. It was found that the scratch speed significantly affects the pile-up and groove depth because of the phenomenon like stress build up and elastic recovery. A complementary analytical model of ploughing and shearing forces developed here led to the observation that the minimum chip thickness can only be around 0.1 to 0.2 times the radius of the indenter. Elastic recovery was found to be larger at the the middle of the scratch, which was confirmed with the stress-strain relations derived from the FEM simulations. It was also observed that the spacing between two subsequent scratches can significantly affect the

scratched surface quality. These experiments show that the severe ploughing and mid-region ridge features can be avoided by having the scratch pitch to be at least one third of the grit tip radius.

Keywords: Grinding; Single scratch test; Cutting force; Pile-up ratio; Sub-surface deformation

1 Introduction

Ti-6Al-4V alloy offers good balance of characteristics, including strength, ductility, fracture toughness, high temperature strength, creep strength, weldability, workability and thermal processing (higher strength can easily be obtained by heat treatment). This alloy is therefore mainly used for airframe and engine parts. Owing to very low thermal conductivity, Ti-6Al-4V behaves differently during machining specifically when machined at micro-scale with rounded edge tools. Generally, materials undergo mechanisms such as, rubbing, ploughing, shearing and prominent elastic recovery (springback) when processed at micro/ nano-scale. Moreover, the mechanisms are largely affected by the chip thickness, abrasive grit shape, cutting speed, infeed angle and cutting environment.

Single grit scratch test has been a very promising approach to understand micro/nanoscale material removal mechanisms and to determine the representative machining or grinding parameters [1, 2]. There are many prior research works where single grit scratch tests were utilized to understand the effect of the processing parameters on the process responses [3].

Matsuo et al. [4] performed single grit scratch tests on SUJ2, S50C, and SS41 steels using diamond and CBN grits on a surface grinder. They used a cutting speed of 12.7 to 30 m/s and maximum depth of cut up to 50 µm. They found that the scratch force increases with the cross sectional area of the grit, and the slope of force lines increases as the apex angle of the single grit increases. They also concluded that the material pile-up along the scratch is largely

dependent on the direction of scratching. Ohbuchi et al. [5] performed a single grit cutting test on a lead workpiece, using well-shaped CBN and diamond grits. Cutting forces were lower and plastic deformation was remarkable when cutting was carried out with the CBN grits. Furthermore, rake angle had a larger effect on the thrust forces as compared to that on the axial cutting forces.

Wang et al. [6] carried out a single grit rotating scratch test on pure titanium using a conical diamond tool. They found that the increase in overall friction coefficient along the scratch was a result of increased attack angle. They attributed the observed fluctuation in friction coefficient to the dynamic characteristics of the scratching process including the contact mechanism between the tool and the workpiece. Subhash et al. [7] performed single grit scratching tests on metals and ceramics to compare material removal mechanisms and to mathematically describe the induced topological features. The evolution of forces in cutting the ductile metal was a smooth sinusoidal curve, and it showed generation of periodic lobs during the cutting of brittle materials. They used Green's function to categorize physical features of the scratch on both types of materials. The ductile flow in metals was represented as heavily damped sinusoidal function, whereas brittle cracking in ceramics was observed as heavily damped multiple oscillatory roots.

Chen et al. [8, 9] simulated grinding with single grit scratching using finite element simulation. They divided the scratch path in three steps and adopted a multi-pass scratch methodology to imitate the effect of abrasive separation distance on a grinding wheel. It was evident that a higher coefficient of friction between grit and workpiece caused larger ploughing ridges and higher cutting forces. Singh et al. [10] compared specific ploughing energy requirement of ductile and ceramic materials using single grit scratching tests. They found that specific ploughing energy was 20% and 25% of the total grinding energy, for mild steel and composite ceramic material, respectively. Opoz et al. [11] investigated single grit grinding with a specially

designed single scratching setup. They defined material removal mechanism in terms of pile-up ratio and chip removal strength. They concluded that the pile-up ratio increases as the grit begins to wear out, and as a consequence, multiple cutting edges comes into action. Cutting was more prominent at the entry side of the scratch, whereas pile-up prevailed at the exit of the scratch. Ghosh et al. [12] performed single grit grinding tests on rolled aluminium using a diamond abrasive grit of size 600 µm. They concluded that an increase in infeed angle of a grit into the workpiece reduces specific cutting energy due to reduced ploughing action. Further, the height of the ploughed or piled-up material was observed to be of the order of 0.7 to 0.8 of the groove depth. Chen et al. [13] observed the chip formation and segmentation mechanisms in single grit grinding on nickel-based superalloy GH4169 using a brazed diamond tip. Chip serration was insignificant up to the cutting speed of 60 m/s, whereas beyond 150 m/s, the chip serration was observed. They found that the chip segmentation frequency changes from 18 MHz to 75 MHz as the cutting speed changes from 60 m/s to 150 m/s. Gao et al. [14] performed micro-scratch tests on copper to understand the effect of normal load on the coefficient of friction. They put forward that the coefficient increases with the normal load and elastic deformation predominates on large normal loads. Material was under hydrostatic compressive stress state during micro-scratching with spheroconical indenter. Gao et al. [15] utilized the constant load micro-scratching to observe the effect of sample tilt on coefficient of friction. They established that the surface tilt has significant effect on the measured coefficient friction value. On changing the tilt angle from -3° to 3°, the coefficient friction changes by three times. Liu et al. [16] compared the micro-scratch response of different metals with progressive normal load between 5 mN to 30 N, using Berkovich and Rockwell C indenters. It was observed that penetration depth and residual depth increase linearly with normal force in case of Rockwell C indenter, whereas, the variation was non-linear in case of Berkovich indenter. Elastic recovery increased at a faster rate initially and then became stable at higher normal loads. Liu [17]

performed constant load scratching on copper using Rockwell C indenter of 105 µm tip radius. Cracking area, penetration depth and residual depth were analyzed to find the fracture toughness of the material. A significant pile-up around the scratch was observed for spherical contact. Energetic size effect law was established as the most suitable for characterizing the fracture toughness of metallic materials using scratch-based approach.

Axinte et al. [18] investigated the effect of abrasive micro-geometry on the cutting mechanism of ductile (copper) and brittle (sapphire) materials, with an objective to develop shaped abrasives in a grinding process. Abrasives grits of circular, triangular and square cross sections were generated on a CVD diamond substrate using laser ablation. The effect of number of cutting edges (NoCE) and cross sectional area in contact on the mechanism of cutting was studied. The higher the active NoCE (in this case for square base frustum), the more localized the plastic deformation is, and more accurate is the replication of the grit shape on the surface of copper. However, cracks and damage on sapphire surface resulted in poor replication of the grit shape. Grits with cutting edges led to a larger reduction in specific cutting forces in comparison to that of the grits with circular base frustum. Wu et al. [19] analyzed mechanical wear of single crystal diamond (SCD) during single grit scratching on Ta12W. SCD with two different crystal orientations SCD_{100} and SCD_{111} was used for comparison. The wear resistance of the SCD_{111} grit was higher than SCD_{100} grit in normal wear situation, whereas scratching life was higher for SCD_{100} grit. They found that the fracture modes of the grits was dependent on the crystallographic orientation and stress tensor [20]. Yiming et al. [21] utilized AE signals to monitor attrition wear of sharp and blunt grits during scratching of AISI4340 steel. They observed that the lower AE signal frequency band of 0-90 kHz depicted friction and a higher frequency of 90-250 kHz depicted material removal. It was found that the AE signal energy diminished rapidly as the grit gets worn out.

Opoz et al. [22] investigated material removal mechanism in Inconel 718 during single grit grinding experiments using CBN grits. They found that pile-up ratio increased with an increase of cutting depth, and the cutting mechanism altered with a change in cutting edge sharpness. Further, dominant shearing was evident at the entry of a scratch, whereas dominant pile-up was seen at the exit side of the scratch. Yiming et al. [23] simulated a single grit grinding process considering fracture based wear of a grit. While using CBN grit on AISI4340 steel, they found that many small cutting edges were formed on the grit due to the fracture wear. Consequently, chip volume reduced as the grit wear progresses due to material removal by the joint action of small cutting edges. Zhu et al. [24] analysed the wear behaviour of PCBN grits by applying fractal theory during single grit scratching of nickel based super alloy Inconel 718. They established two forms of wear of PCBN grits such as 'micro-fracture' and 'attrition wear'. The micro-fracture was induced by the extension of cracks, whereas attrition wear was the result of adhered grinding chips on the grit surface. Setti et al. [25] performed single grit scratch tests on AISI 1015 steel and 2017A-T4 aluminium alloy to investigate grinding mechanism and cutting regimes. They observed that the minimum chip thickness, besides being dependent of the grit-workpiece material combination, increases at the exit side of the scratch at higher depths of cut. Aluminium 2017A-T4 alloy having higher thermal diffusivity than the Si_3N_4 grit, showed more ploughing than the AISI 1015 steel. Zhao et al. [26] investigated the material removal mechanism of aggregated CBN grits (AcBN) during grinding of Ti-6Al-4V. Aggregated CBN grits could provide finish machined surface due to excellent self-sharpening property and open pore structures of AcBN. Zhao et al. [27] also observed plastic flow on the machined surfaces during ultrasonic assisted roller burnishing of Ti-6Al-4V. It was found that pile-up and deformation were the primary material flow mechanism and there was a minimal change in the workpiece height after burnishing. Wang et al. [28] studied chip formation and surface generation mechanisms considering progressive wear of a cermet tool. The main forms

of surface defects were feed marks, metal debris, plastic side flow, smeared material, and grooves. The cross-sectional geometry of the chip was serrated, the minimum chip thickness was 6.31 μm, and the segment degree was 0.24. A transition from α-Ti to the β-Ti occurred with the tool wear progression in micro-chips. Chen et al. [29] performed high speed cutting of Ti-6Al-4V and observed material removal mechanism in relation with time-dependent micro-structural variation. Ductile shear parabolic dimples and tensile ellipsoid dimples were observed in the free surface of segmented chips in u-HSC of Ti-6Al-4V alloy, which indicated co-existence of severe shear and tensile plastic deformation along the ASB and the free surface of segmented chips.

In conclusion, majority of the studies discussed above are on using single scratching methodology on ductile steel grades and a few on ceramics. Cutting force and surface morphology were studied as a function of cutting parameters. It was evident that shearing prevails at the entry of the scratch and extensive ploughing occurs at the exit side of the scratch. Material pile-up behaviour as a function of grit shape and cutting speed was studied in detail. However, the minimum chip thickness and sub-surface deformation, and their correlations with cutting speed (strain rate) were not addressed adequately, specifically in case of Ti-6Al-4V. In light of this, micro-scale scratching of Ti-6Al-4V seems very important, owing to its unique material response to different strain rates. Moreover, there is no significant work done on the simulation of material removal and surface generation mechanism using multi-scratch strategy which is a key to establish an improved framework for grinding wheel design and process parameter selection. Elastic recovery is another very important mechanism taking place during grinding with large radii tools. Quantification of elastic recovery across the tool-workpiece contact zone needs to be derived as it ultimately contributes in generating the final textures and roughness of the machined surfaces.

Therefore, this work investigates scratching process to understand the material removal regimes and the underlying mechanisms. Particularly, the effect of cutting speed and the scratch separation distance on scratch morphology, cutting mechanism evolution, cutting forces and material deformation were analysed using an improved scratch methodology. Finally, FEM analysis was used to reveal the variation in elastic recovery across the cross-section of grit-workpiece contact area. In light of these aspects, a correlation between grit radius and effective grit spacing was obtained which will aid to obtain an improved understanding about shearing and material pile-up due to ploughing.

2 Experimental methodology

2.1 Theme of experiments

Two types of scratching experiments including single scratch and adjacent scratches were performed in this study (see Figure 1). Both types of experiments were intended to provide unique insights into the material removal regimes during rubbing, ploughing and cutting regions. These experiments also yielded the influence of different scratching parameters on scratched surface profiles. The successive adjacent scratches were made to particularly understand the process of surface generation with respect to successive scratch positions.

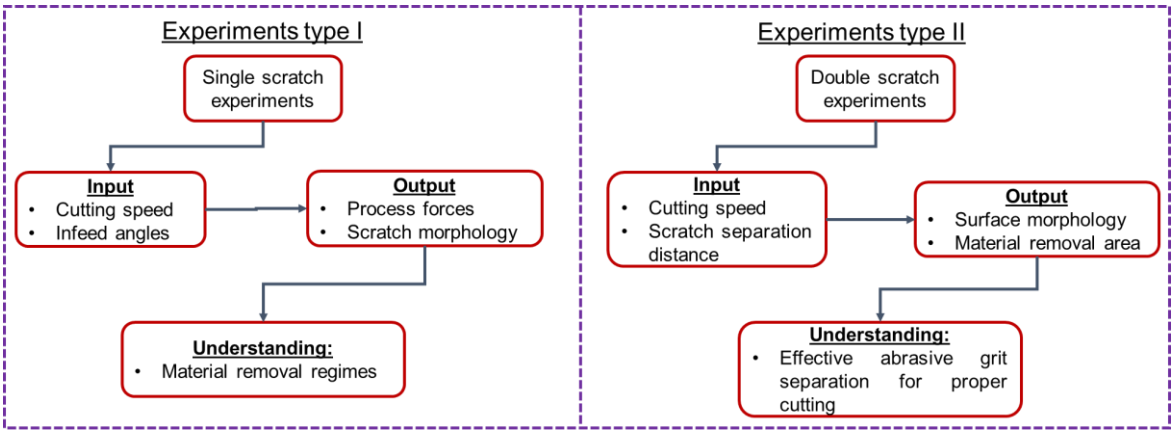

Figure 1. Theme of experiments planned in this work

2.2. Microscratch test setup

Single grit scratch tests were performed on a hybrid micromachining centre DT110 which has a resolution of 0.1 µm and position accuracy of ±1 µm. A special attachment was designed and fabricated to hold the scratching tool and to perform the scratching tests on the machine (see Figure 2). A Kistler mini dynamometer 9657C2 placed below the workpiece was used to record the scratching force signals along the scratch direction and perpendicular to it. Dynamometer signals were also used to set the initial touch point between the scratching tool tip and the workpiece. The scratching tool was slowly fed downward and the force signals were recorded. A zero point was set at the location which showed a sudden rise in the force signal.

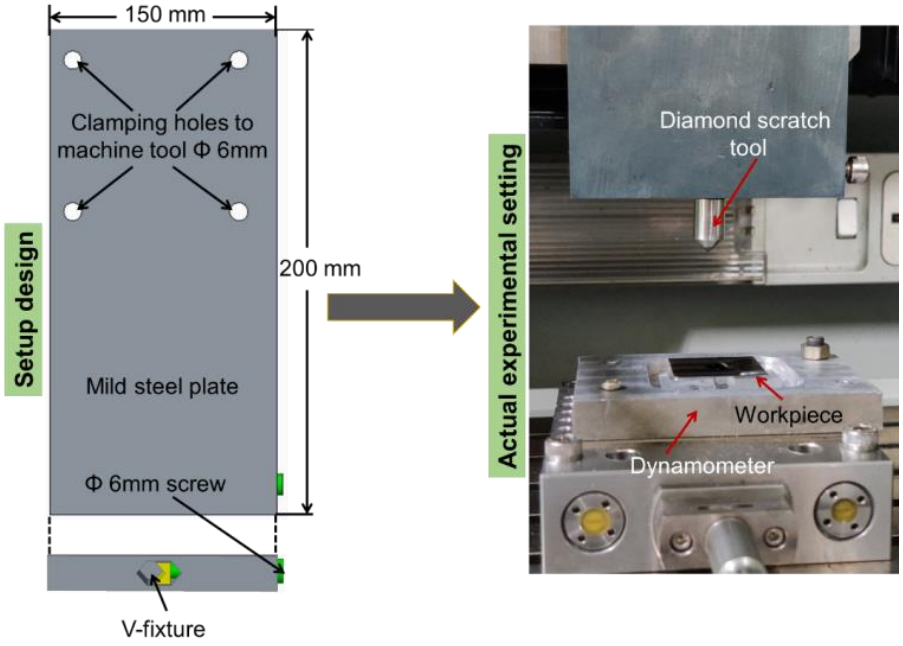

Figure 2. Microscratch test setup

2.3 Materials and methodology

A diamond scratching tool (similar to an indenter) was selected for the experiments. Tip radius and cone angle of the grit were measured using an Alicona 3D profilometer and these were estimated as 120 µm and 90°, respectively (see Figure 3). The workpiece material used was titanium alloy Ti-6Al-4V. Prior polishing of the workpiece on both sides was done to suppress the possibilities of variation in the depth of cut during scratching. Each scratching cycle

included traversing the tool through an increasing-decreasing depths of cut cycles to imitate the grinding process, as shown in Figure 4. The maximum depth of scratched groove goes up to 40 µm. As this is a scratching process with only linear motion of the scratch tool, groove depth and chip thickness are equivalent to each other.

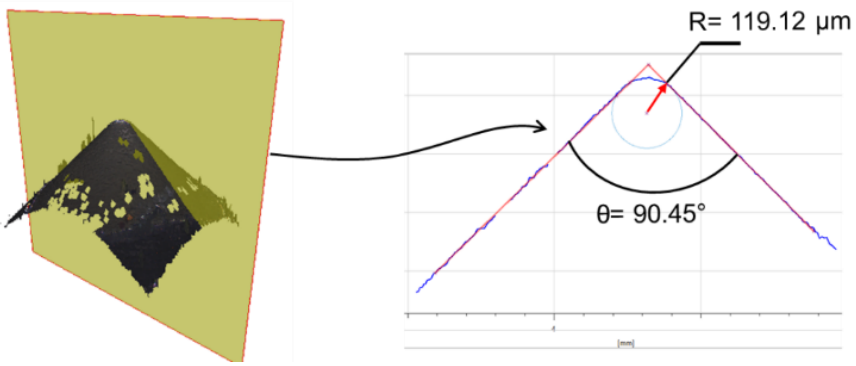

Figure 3. 3D profile and section measurement of the diamond grit

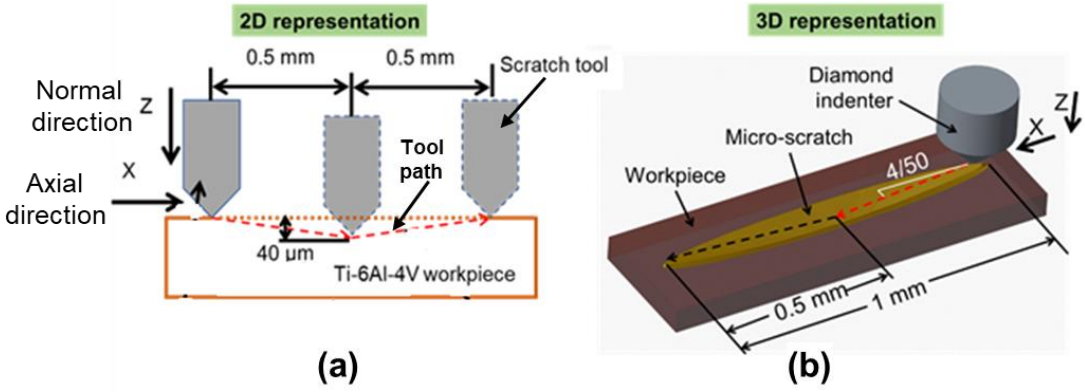

Figure 4. Scratching methodology illustrated (2D and 3D representation)

To analyse the material removal mechanism and the influence of processing parameters, various exploratory experiments were performed. In the first instance, single scratching experiments were done to understand the effect of cutting velocity on the material removal behaviour, see Figure 4(a). Secondly, adjacent scratches were made by varying the pitch (spacing between the scratches) to analyse the effect of grit spacing on the material removal behaviour. The range of experimental parameters used are presented in Table 1. An exploratory experimental design involving two types of scratch experiments is presented in Table 2. The

first five experiments were single scratching experiments at varying cutting speeds of 20 mm/min to 160 mm/min. Another five experiments were adjacent scratches performed at a constant cutting speed of 80 mm/min and with varying scratch spacing between 10 to 150 µm.

Table 1. Scratching parameters range

Parameters	**Range**
Cutting speed (v_c)	Varied from 20 to160 mm/min
Maximum scratch depth	40 µm
Scratch slope (Z/X)	4/50
Separation distance (l_s)	Varied from 10 to 150 µm

Table 2. Experimental design for three types of scratch

Experiment type/ No	**Fixed parameters**	**Varying parameter**
Single scratch	Scratch slope= 4/50	Cutting speed v_c (mm/min)
1		20
2		40
3		80
4		120
5		160
Double scratch	Cutting speed (v_c)= 80 mm/min	Separation distance (µm)
1	Scratch slope= 4/50	10
2		40
3		90
4		120
5		150

2.4 Scratch profile measurement and the criterion for differentiating material removal mechanism

Scratch profiles were measured using an Alicona 3D profilometer. Typical profiles and geometric features of scratches on work surfaces are shown in Figure 5. Using 3D profile measurements, 2D sectional profiles were extracted at different locations along the length of scratches to quantify groove areas, scratch depths and pile-up areas. A typical 2D profile along the cross section of the scratch is shown in Figure 6. Different parameters were defined to quantitatively compare material removal mechanisms under different scratching parameters. A typical groove cross sectional area and pile-up areas are shown in green and red colours (based on the general consensus of desirability; green refers to desirable (GA), red refers to

undesirable (PA_1+PA_2). More pile-up indicates dominant ploughing effect, whereas larger groove area represents active cutting or shearing. In case of large radius tools, material deforms plastically without complete chip formation when the depth of cut or chip thickness is small. This region is termed as ploughing-dominant region. As the chip thickness goes past a threshold value, the chip formation begins and the material removal regime transitions into the shearing-dominant mode. Parameters such as "Pile up ratio" and "Material removal area" were defined to compare the material removal abilities under different scratch conditions. The following conditions were adopted to categorize the material removal mechanisms as ploughing dominant or shearing dominant:

$PA_1 + PA_2 = GA = 0 \qquad Pileup\ ratio: \infty \qquad Rubbing$

$PA_1 + PA_2 > GA \qquad Pileup\ ratio: > 1 \qquad Ploughing\ region$

$PA_1 + PA_2 = GA \neq 0 \qquad Pileup\ ratio: 1 \qquad Elastic - plastic\ Transition$

$PA_1 + PA_2 < GA \qquad Pileup\ ratio: < 1 \qquad Shearing\ (Plastic\ flow)$

Effective grit engaging radius (R_e) was also measured which is a nominal grit radius in contact with the workpiece at an instance. In other words, R_e is the radius of the scratched groove. The theoretical radius of the scratched groove should be equal to the radius of the indenter or scratch tool, but the actually achieved radius of the scratched groove will be different due to the inevitable elastic recovery of the material. This parameter could be measured using the scratch profile as shown in Figure 6.

Open-source software ImageJ was used to measure the pile-up areas and groove section areas. ImageJ offers direct tools for selection and measuring the areas. First, scale of the image should be set using 'Set scale' tool. After that, the area of focus was selected using 'Freehand selection' tool and then measured using 'Measure' tool available in the GUI. Also, the morphology of scratched grooves was observed using scanning electron microscopy (SEM). These measurements helped understand the material deformation behaviour better.

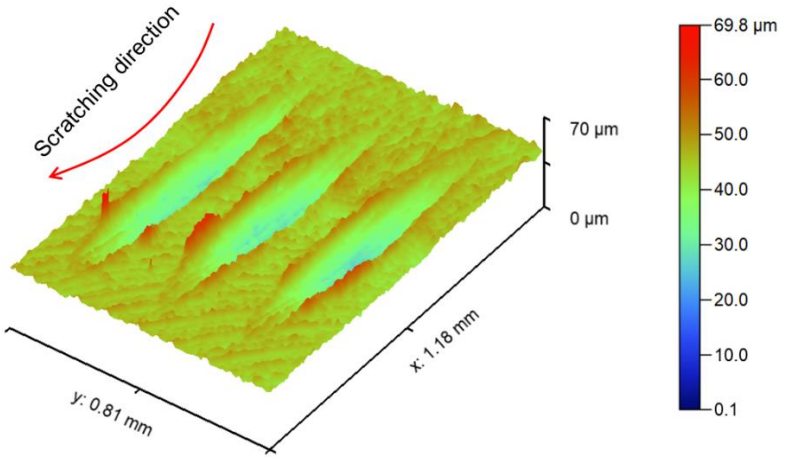

Figure 5. Measured 3D profile of typical scratches

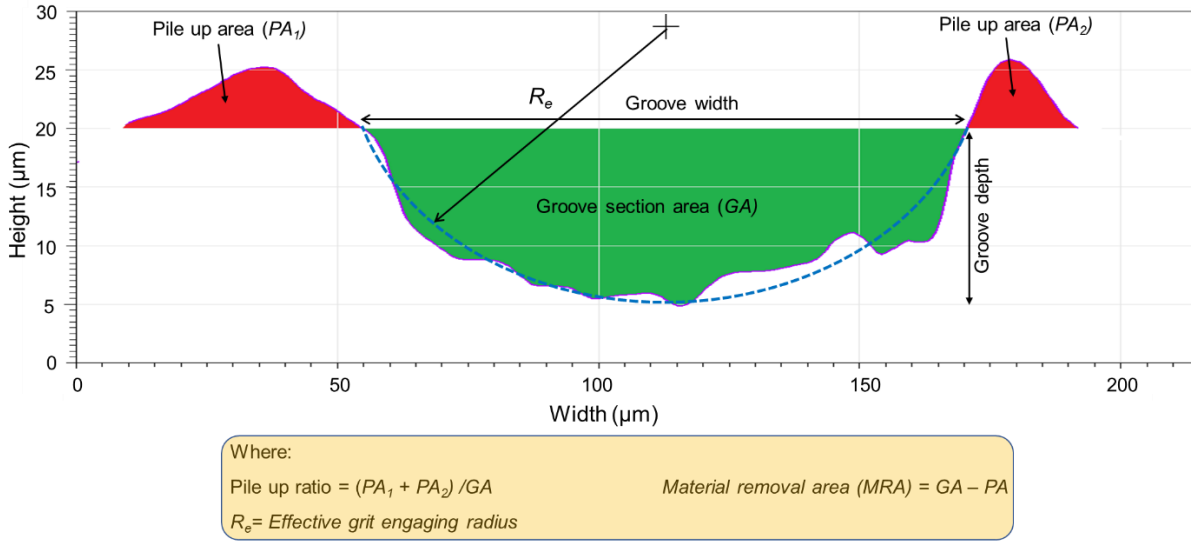

Figure 6. 2D section profile of a typical scratched groove

3 Results and discussion

3.1 Material removal mechanism during single scratching

3.1.1 Cutting forces

Scratch force signature (the orthogonal forces, F_x and F_z) at cutting speed of 80 mm/min is presented in Figure 7(a). Maximum normal force *Fz* was almost double in magnitude than the cutting force F_x. The forces increase up to the halfway of the scratch path and begin to reduce, when the tool retracts from the workpiece in the later half. It was noticed that the force profiles were smoother in the first half as compared to that of the second half.

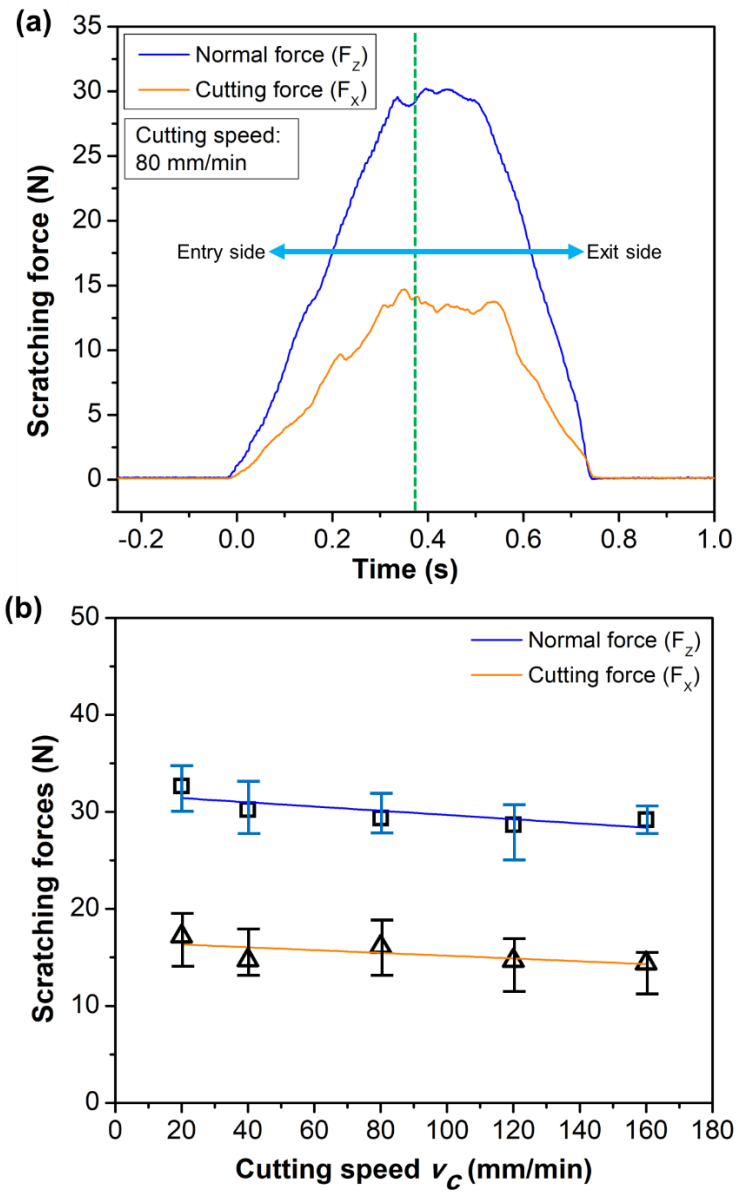

Figure 7. (a) Scratching force signature and (b) scratching force variation with respect to cutting speed

The forces did not reduce suddenly after changing their path towards the exit side rather they remain fairly constant over some distance and then begin to decline. A similar trend was also observed in a related study [30]. The reason behind this could be the accumulation of ploughed material in front of the grit. As the grit penetrates into the workpiece in the first half of the scratching path, material accumulation in front of the grit goes on increasing. During exit from the workpiece in the second half of the scratching path, the accumulated material obstructs the tool movement. This increases the force for retraction. At a point, where the grit overcomes the material resistance, and the material flows sideways, the forces start declining. Another

important observation can be made about the slope of the force curve on the entry and exit side. On the entry side, the slope of the force curve was more gradual as compared to the steeper slope on the exit side. It means that the forces at a given depth on the exit side were higher in comparison to the entry side.

The peak scratch forces at various cutting speeds are plotted in Figure 7(b). It was observed that the forces vary inversely with increasing cutting speed i.e., higher speeds lead to lower forces. This can be explained by the predominant thermal softening (high strain rates) as opposed to strain hardening (low strain rates).

3.1.2 Material removal mode and minimum chip thickness determination

Material pile-up along the groove length is a good indicator of material removal behaviour. Therefore, pile-up ratio along the scratch path or groove length is plotted in Figure 8(a). The pile-up ratio appears to be asymmetric but differs at the entrance and the tool exit. For instance, at the beginning of the scratch it is higher, but gradually decreases towards the middle of the scratch, and finally increases to a higher value at the end of the scratch. In the initial stages, when the depth of cut is low, the chip removal did not occur, rather ploughing phenomena prevailed due to dominant 'size effect'. As a result, large material pile up and higher pile up ratio were evident.

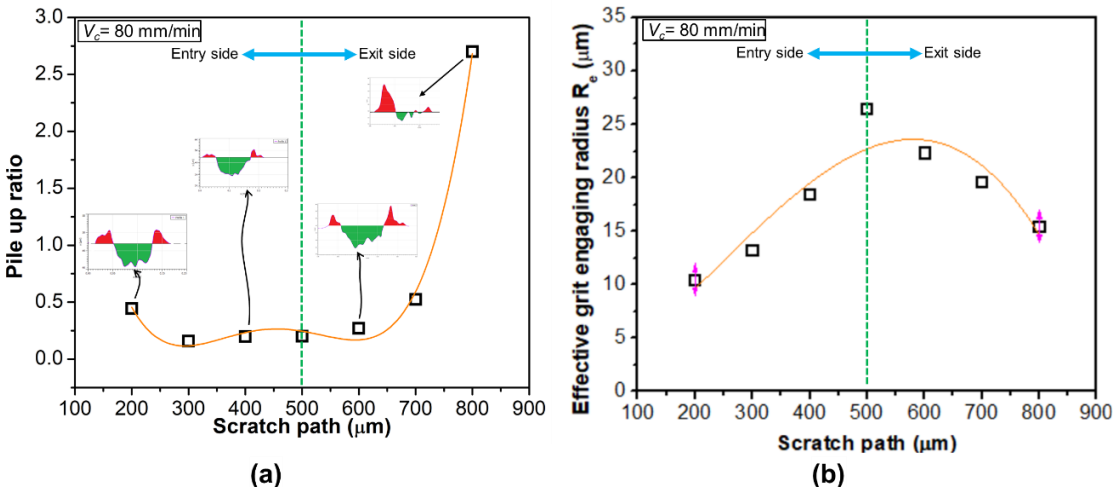

Figure 8. (a) Pile up ratio variation and (b) effective grit engaging radius along the scratch path at cutting speed $v_c = 80$ mm/min

As the scratch proceed, the depth of cut increases, material removal in the form of chips prevails and pile up ratio becomes smaller. On the exit side of the scratch, similar phenomenon occurs and the pile-up ratio increases towards the end of the scratch due to reduced depth and a dominant ploughing. Moreover, the pile-up ratio on the exit side of the scratch become far higher than what it is at the entrance. The additional material pile-up on the exit side can be attributed to the continuous material accumulation in front of the grit, resulting in the pile up along the groove side. The effective grit engaging radius along the scratch path was also plotted and it is shown in Figure 8(b). It was found to increase along the scratch length. Small grit engaging radius allows easy flow of material in upward direction. Therefore, pile-up was more at lower depth of cut owing to small grit engaging radius, which is also evident from the schematic shown in Figure 8(a). As depth of cut increases, grit engaging radius also increases and upward material flow was suppressed.

The material removal mechanism and minimum chip thickness were further classified based on the conditions stated in section 2.4. Pile-up ratio along the entire scratch path is plotted with respect to the groove depth or chip thickness at various cutting speeds (see Figure 9(a-c)). Pile-up ratio for entry and exit sides of the scratch are plotted separately in a single view to clearly distinguish the material removal mechanisms. The pile-up ratio and material removal regimes for cutting speed of 80 mm/min are shown in Figure 9(a). There was no ploughed material or groove observed for the chip thickness in the range of 5 to 6 µm and instead this was seen to lead to a higher pile-up ratio. Therefore, this region was categorised as rubbing region, where almost complete elastic recovery took place without any significant permanent deformation in the work material. Further increase in the chip thickness led to increase in both pile-up area and groove area. However, increase in pile-up (PA) was significantly higher in comparison to

the groove area (GA). Pile-up ratio (PA/GA) in this region was greater than 1, which suggests that the material removal mechanism can be placed into ploughing dominant region. The phenomenon continues until the chip thickness of 13 µm. Beyond the chip thickness value of 13 µm, pile-up ratio (PA/GA) was less than 1. Therefore, the material removal mechanism was confirmed as shearing dominant cutting, in view of the criterion defined in Section 2.4. Hence, the minimum chip thickness (h_m) at the cutting speed of 80 mm/min was established as 13 µm (see Figure 9-a). When the chip thickness was larger than 13 µm, the pile-up ratio goes below 1 and the material removal enters into the shearing dominant regime. Observing the geometry of scratch on the exit side, this regime of material removal persists till the chip thickness of 28 µm, and thereafter, severe ploughing is observed. The pile-up ratio increases drastically due to significant work material accumulation in front of the grit. This analysis shows that the material removal mechanism and regions thereof were quite different for up-grinding and down-grinding processes.

Analysis of the material removal mechanism at low cutting speed of 20 mm/min (Figure 9(b)_ and high cutting speed of 160 mm/min (Figure 9(c)) shows that the minimum chip thickness is influenced by the material pile-up behaviour and its dependence on the cutting speed. The pile-up ratio at the deepest location of the grooves at different cutting speeds is plotted in Figure 10. The pile-up ratio is higher at low cutting speeds due to low temperature in the machining surface and sub-surface which results in low diffusion constant of the partial dislocation of titanium alloy and reduced. Therefore, dislocations may not fully jump out of the intrinsic planes and quantity of immobile defects could be high. As a result, complete shearing may not take place instead material pile-up would happen. An increase in the cutting speeds gives rise to the increase of temperature in the cutting zone which eases material flow and reduces pile-up. On further increasing the cutting speed beyond 80 mm/min, the pile-up increases again which may be attributed to strain rate hardening near the grain boundaries [31].

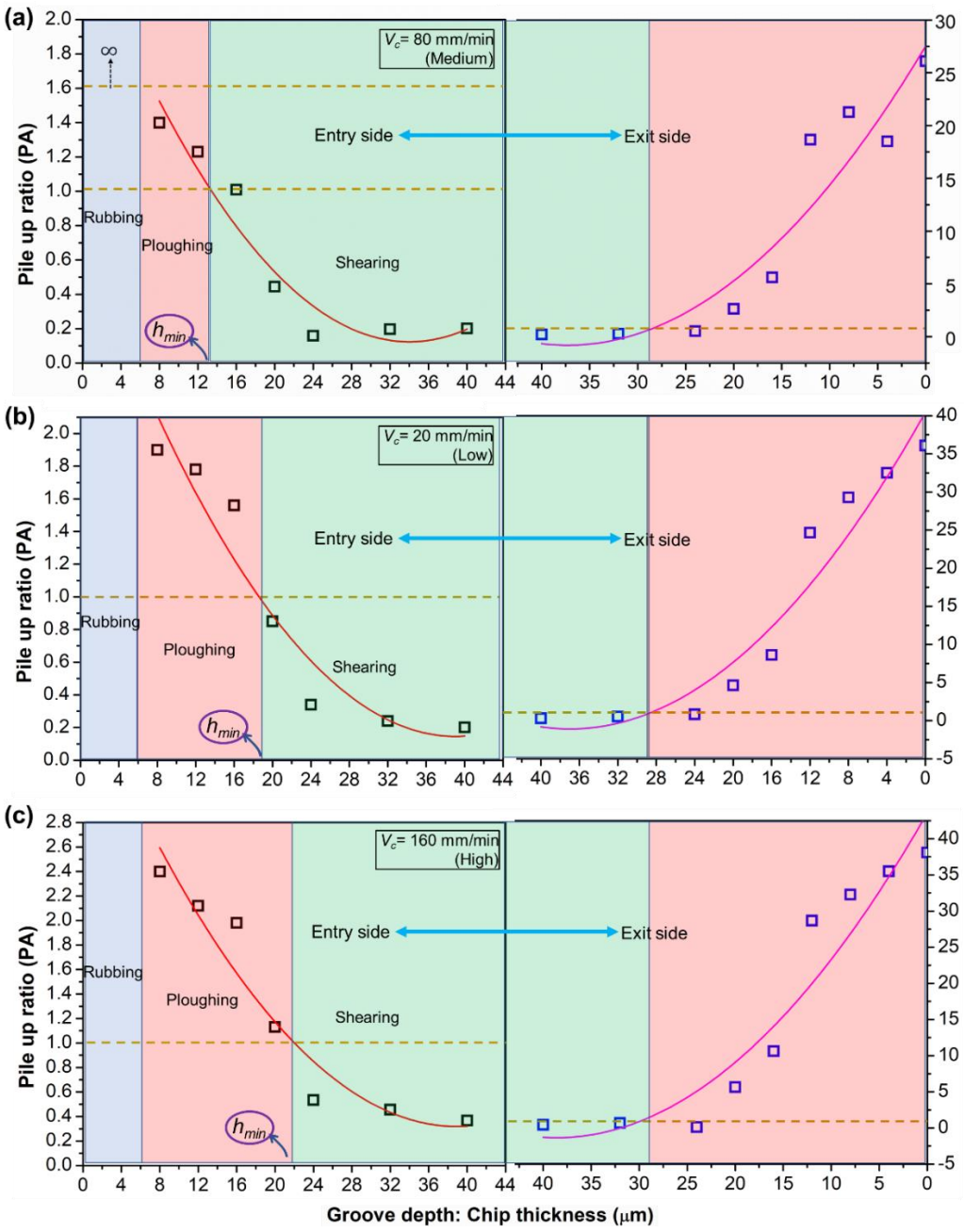

Figure 9. Classification of material removal regimes as a function of chip thickness

Based on this analysis of pile-up behaviour, the material removal regimes at different cutting speeds can be identified. As the pile-up tendency is more at low cutting speed of 20 mm/min, the ploughing dominant region increases, and therefore the minimum chip thickness increases to 19 μm in comparison to that of 13 μm at the cutting speed of 80 mm/min. Similar trend was observed for the cutting speed of 160 mm/min, where minimum chip thickness increases to 22

μm. It is therefore evident that the minimum chip thickness (h_m) is in the range of 0.1-0.2 *R*, where, *R* is the tip radius of the grit (*R*= 120 μm in the current experimental work).

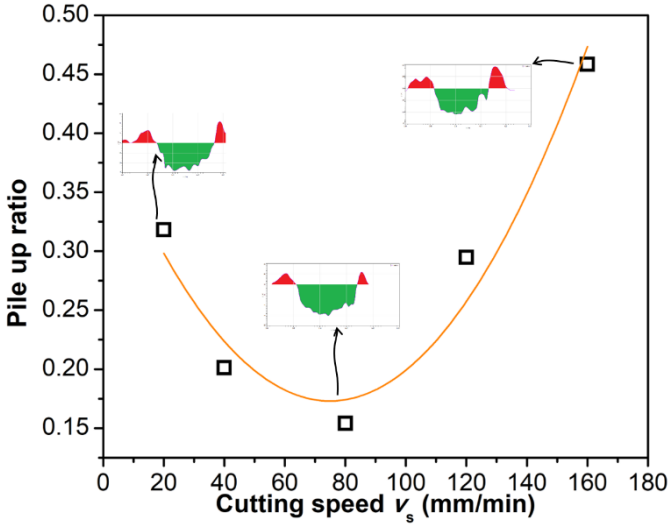

Figure 10. Pile-up ratio variation with respect to cutting speed

3.1.3 Analytical prediction of minimum chip thickness

The scratching experiments have shown that the mode of material removal depends strongly on chip thickness. Grinding or milling processes entail multiple scratches on a surface formed by multiple grits or tool cutting edges. In previous research, analytical model of grinding process was accomplished based on the analysis of single abrasive grit scratching [32] and more recently, machine learning approaches have been proposed [33].

In this work, an analytical model of forces has been developed for establishing the mode of material removal in scratching such that it distinguishes ploughing and shearing, see schematic in Figure 11 (a). A spheroconical indenter of tip radius *R*, acts as a tool, is in contact with the workpiece surface. The cutting parameters on this stage were cutting depth of *t*, rake angle of the tool α, shear angle ϕ and friction angle β. F_C and F_T denote axial (feed) force and normal (tangential) force, respectively. Merchant's orthogonal cutting model [34] was considered applicable here to calculate shear forces, and a separate indentation model was considered to account for the ploughing action caused by the radius of an indenter. Merchant's model is

generally applied when a wedge type of tool makes a flat-faced contact with the workpiece. Whereas, the grit used in the present work is of sphero-conical shape which makes hemi-spherical contact with the workpiece. In order to use Merchant's model for our case, only projected area of the grit has been considered for the analysis. It is assumed that the workpiece is making contact with the plane projected area of the hemi-spherical grit as shown in Figure 11(b).

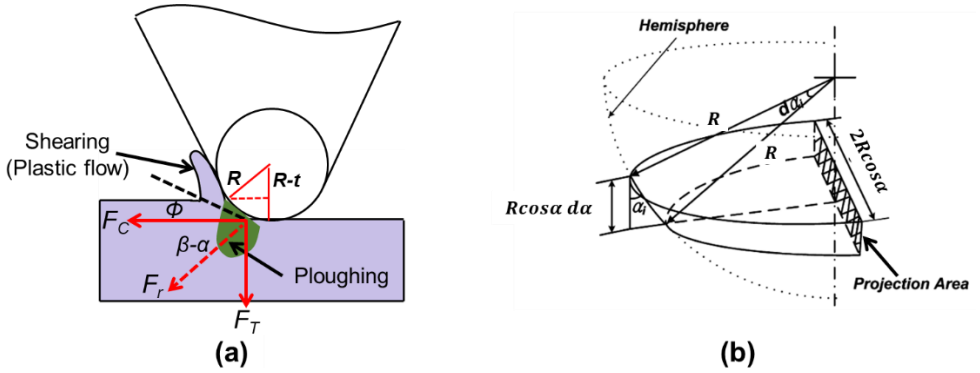

Figure 11. (a) Geometrical model of scratching with sphero-conical indenter and (b) elemental area of hemispherical part of the grit in contact with the workpiece

There are two distinct modes of material removal viz., ploughing and shearing. The ploughing refers to elasto-plastic deformation of the material when depth of cut is below the minimum chip thickness. The shearing refers to material removal caused by the flow stress leading to the formation and flow of cutting chips above a certain critical chip thickness. Shear forces were calculated based on Merchant's model of orthogonal cutting [35] as:

$$dF_{C,\ s} = \frac{\tau_s \cos(\beta-\alpha)}{\sin\emptyset\ \cos(\emptyset+\beta-\alpha)} dA \quad (1)$$

where, dA is the elemental projected area of the indenter in contact with the workpiece. A sphero-conical indenter was used in the present scratching study. A geometric model of the hemispherical part of the grit in contact with the workpiece is shown in Figure 11(b). The elemental projected area of contact (dA) can be expressed as:

$$dA = 2R^2 cos^2\alpha\ d\alpha \quad (2)$$

The shear angle $\emptyset$ can be expressed as [35]:

$$2\emptyset + \beta - \alpha = \frac{\pi}{2} \tag{3}$$

Therefore, shear forces are given by:

$$F_{C,\ s} = \int_0^{\sin^{-1}\frac{R-t}{R}} \frac{2\tau_s \cos(\beta-\alpha)}{\sin(\frac{\pi}{4}-\frac{\beta}{2}+\frac{\alpha}{2})\cos(\frac{\pi}{4}-\frac{\beta}{2}+\frac{\alpha}{2})} R^2 cos^2\alpha\ d\alpha \tag{4}$$

Normal force component due to shearing can be written as:

$$dF_T = dF_c \tan(\beta - \alpha) \tag{5}$$

$$F_{T,\ s} = \int_0^{\sin^{-1}\frac{R-t}{R}} \frac{2\tau_s \sin(\beta-\alpha)}{\sin(\frac{\pi}{4}-\frac{\beta}{2}+\frac{\alpha}{2})\cos(\frac{\pi}{4}-\frac{\beta}{2}+\frac{\alpha}{2})} R^2 cos^2\alpha\ d\alpha \tag{6}$$

Now, the force components due to ploughing in the two orthogonal directions can be written as:

$$F_{C,\ p} = \int_0^{\sin^{-1}\frac{R-t}{R}} 2\mu_p \sigma_c cos(\beta_i - \alpha_i) R^2 cos^2\alpha\ d\alpha \tag{7}$$

$$F_{T,\ p} = \int_0^{\sin^{-1}\frac{R-t}{R}} 2\mu_p \sigma_c sin(\beta_i - \alpha_i) R^2 cos^2\alpha\ d\alpha \tag{8}$$

where, μ_p is the ploughing friction coefficient which can be written as [36]:

$$\mu_p = 2\ \frac{R^2 cos^{-1}\left(\frac{R-t}{R}\right) - (R-t)\sqrt{P_0(2R-t)}}{\pi(2Rt-t^2)} \tag{9}$$

Force components due to shearing and due to ploughing were obtained by solving equations 4, 6 and 7, 8. The force components in two orthogonal directions, due to shearing and ploughing, with respect to chip thickness are presented in Figure 12(a)-(d), respectively. Both forces were observed to scale with the increase of the chip thickness. To calculate the relative contribution of ploughing and shearing, the contribution factors of the forces were estimated. The relative contribution of the shearing force in the axial direction is given by:

$$C_{C,\ s} = \frac{F_{C,\ s}}{F_{C,\ s} + F_{C,\ p}} \tag{10}$$

Similarly, the relative contribution of ploughing forces in the axial direction is given by:

$$C_{C,\ p} = \frac{F_{C,\ p}}{F_{C,\ s} + F_{C,\ p}} \tag{11}$$

and that of the shearing and ploughing forces in the normal direction were obtained respectively as:

$$C_{T,\ s} = \frac{F_{T,\ s}}{F_{T,\ s} + F_{T,\ p}} \tag{12}$$

$$C_{T,\ p} = \frac{F_{T,\ p}}{F_{T,\ s} + F_{T,\ p}} \tag{13}$$

Modeled force values and their relative contributions are determined by simulating the equations 4-13 using MATLAB. Important properties of Ti-6Al-4V required to simulate these equations are provided in Table 3.

Table 3. Physical properties of Ti-6Al-4V

Property	Density, ρ (kg/m$^{3)}$	Elastic modulus, E (GPa)	Poisson's ratio, ν	Shear strength, τ_s (MPa)	Compressive strength, σ_c (MPa)
Value	4430	110	0.33	760	848

The relative contributions of ploughing and shearing forces in the axial and normal directions are plotted in Figures 12(e) and 12(f). It is noted that the contribution of ploughing force is larger at low chip thickness, whereas the forces in the shearing regime begin to dominate when the chip thickness goes past 12.55 and 11.67 µm. Therefore, minimum chip thickness h_{min} in this case, is approximately established to be between 11.5 to 12.5 µm which is about 0.1 to 0.2 *R*, where *R* is the tip radius of the grit (*R*=120 µm in the present case). This is corroborated with the experimentally determined values of chip thickness.

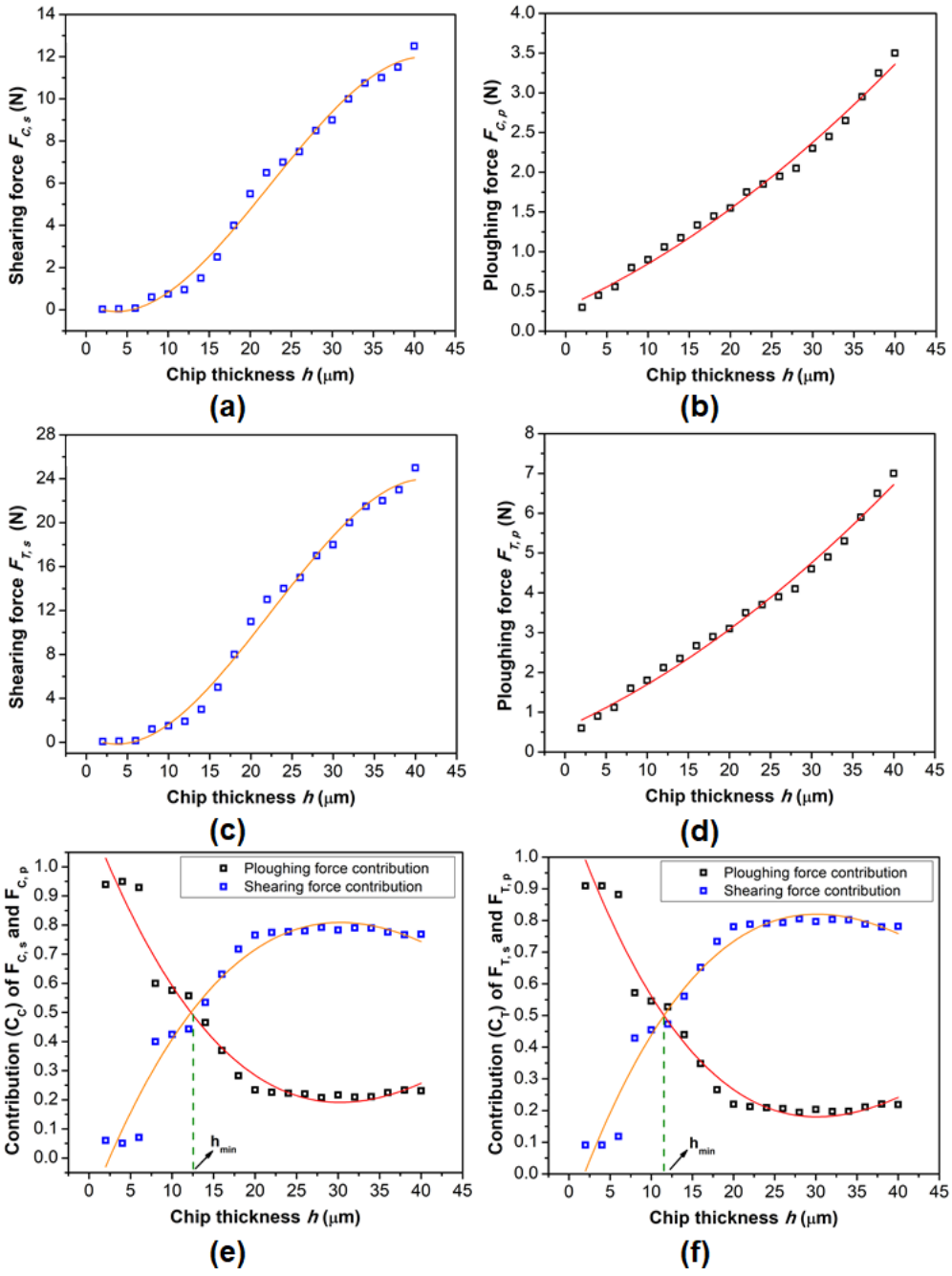

Figure 12. (a)-(d) Predicted shearing and ploughing force variation with chip thickness in axial and normal direction, (e)-(f) contribution of ploughing and shearing forces on varying chip thickness

3.1.4 Scratch topography, elastic recovery and sub-surface deformation

The groove depth measured at the deepest point on the grooves is plotted in Figure 13. It is well known that the measured depth is always shallower than the programme depth of cut due to the dynamic elastic recovery which was recently estimated as a function of depth of cut [2]. The groove depth showed a decreasing trend with respect to the cutting speed which implies that the amount of elastic recovery is more at higher cutting speed. The general perception for

ductile materials, like steel and aluminium is that an increase in strain rate associated with high cutting speed leads to a higher flow stress. The higher flow stress is realized due to multiplication of dislocations inside the material. Thus, the change in the material structure due to multiplication of dislocations could lead to a lower elastic recovery. Titanium alloy Ti-6Al-4V behaves contrary to this, which could be attributed to the low thermal conductivity of Ti-6Al-4V. It results in further lowering of Young's modulus with increasing strain rate or cutting speed. As the modulus goes down, yield strength of the material rises and higher elastic recovery could be observed [37]. Therefore, the measured groove depth at higher cutting speeds is lower as compared to that at the lower cutting speeds.

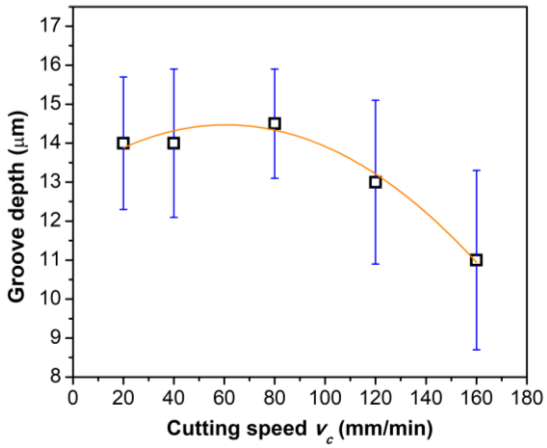

Figure 13. Groove depth of scratches formed at various cutting speeds

Another important phenomenon on elastic recovery was observed across the cross section of the scratched groove. It was noticed that the elastic recovery was not uniform across the cross section. Calculation of theoretical groove profile (for 120 μm radius sphero-conical indenter and 40 μm scratching depth) is shown in Figure 14(a). A comparison of theoretical and experimental profiles of the scratched groove is shown in Figure 14(b). Representation of the elastic recovery $'h_e'$ at three locations P_1, P_2 and P_3 is also shown in the same Figure 14(b). Amount of h_e was highest in the middle of cross section and decreased towards side walls.

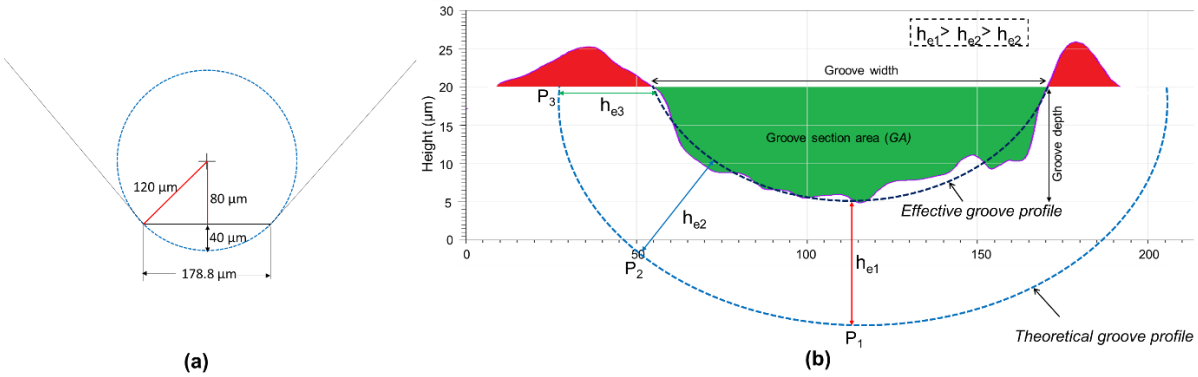

Figure 14. (a) Calculation of theoretical groove profile, (b) elastic recovery across the cross section of a typical experimentally scratched groove

To confirm this behaviour, finite element analysis of scratching was performed in Abaqus/explicit^{TM}. Tool-tip was assumed to be rigid, whereas the workpiece was modelled as elastoplastic material including damage evolution. Further, the workpiece was discretized with 3D stress elements (C3D8R) and the mesh was refined in the scratching area. For the purpose of brevity the simulation details are not repeated but these details including constitutive model, boundary conditions, etc can be seen from elsewhere [38]. A typical scratch obtained in the simulation is shown in Figure 15. The scratch, accumulated material in front of the tool-tip, and broken chips are clearly visible in Figure 15. Further, the cross section of the scratch obtained in the simulation is shown in Figure 16(a). On the cross section, at the outer boundary of the scratch, three material points P_1, P_2 and P_3 were selected for stress-strain analysis. The equivalent stress-strain curves for the aforementioned three points are plotted in Figure 16(b). Point P_1 underwent largest strain and offered higher resisting stresses, because this point was under large compression underneath the tool tip. However, stress and strain magnitudes became smaller for points P_2 and P_3. From the stress-strain curves, elastic recoveries for the points could be deduced as

$$h_{e1} = L_1 tan\theta, \quad h_{e2} = L_2 tan\theta, \quad h_{e3} = L_3 tan\theta$$

Since, $L_1 > L_2 > L_3$

Therefore, $h_{e1} > h_{e2} > h_{e3}$

This justifies the experimentally observed trend of elastic recovery variation across the scratch cross section.

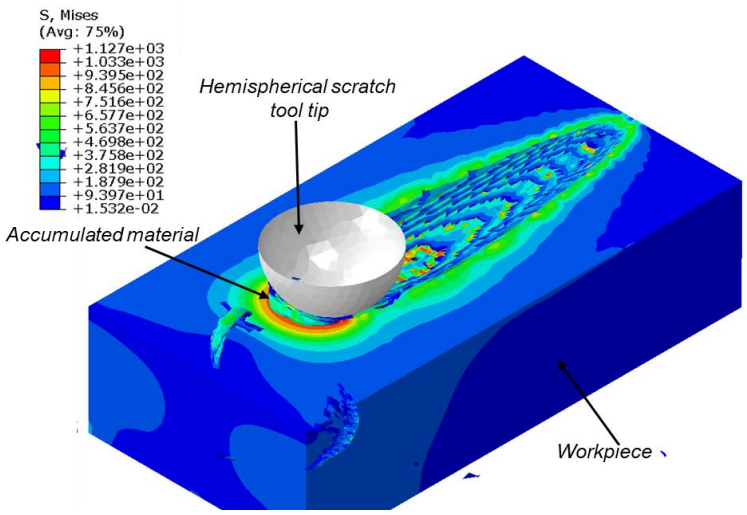

Figure 15. Simulated single scratch in FEM

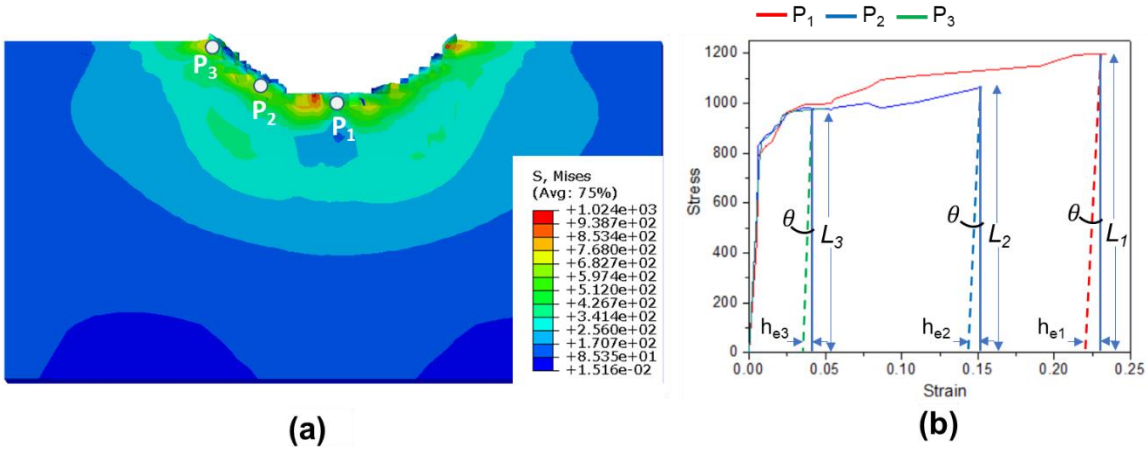

Figure 16. (a) Node selection across the cross section, (b) stress-strain curves and elastic recovery at nodes P_1, P_2 and P_3

Micrographs of scratches taken at different cutting speeds are shown in Figure 17(a)-(e). A detailed analysis of a single scratch groove is further illustrated in Figure 18. Surface morphology of the scratch showed a significant variation along the scratch length and across the cross section. It was noted that there is no material accumulation at the start of the scratch and clean cutting took place. Material pile-up along the scratch begins as the scratching

progresses and the depth of cut increases [39]. When the scratching path reverses, and the grit begins to come out of the work material in the second half, similar scratch morphology is not evident. Instead, a higher material pile-up and dragging occurs. Further, the accumulated material remains on the work surface at the end of scratch. Surface features also varied across the scratch cross section. Smooth surface could be observed in the middle of the scratch cross section. This middle region was in compression against the sharp tool tip and there was a point contact between the tip and the workpiece. In the side regions, hemi-spherical part of the scratch tool was in contact with the workpiece and the work surface slides against the tool surface for a longer duration. This results in material dragging and smearing of the machined surface in this region.

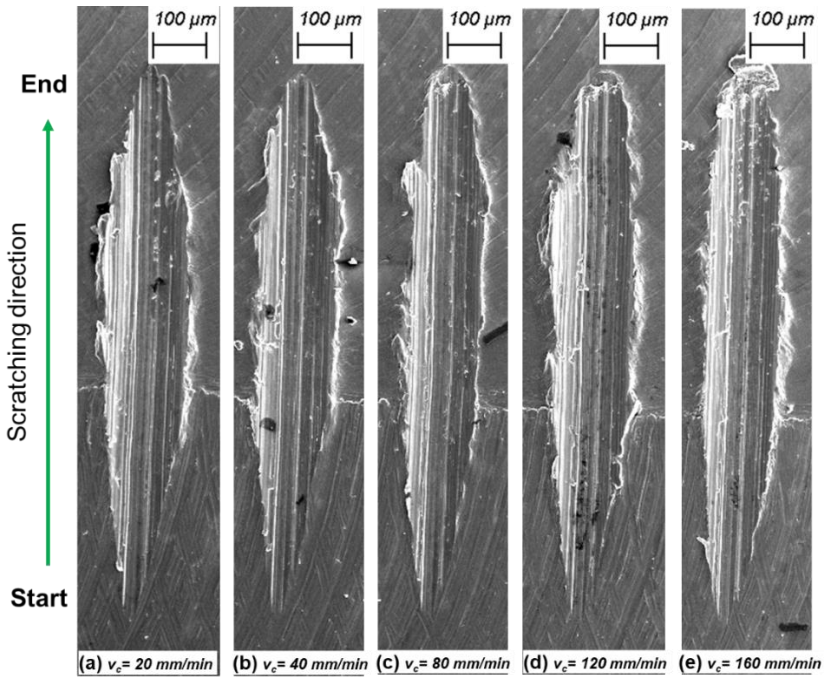

Figure 17. Micrographs of different scratches obtained at varying cutting speeds

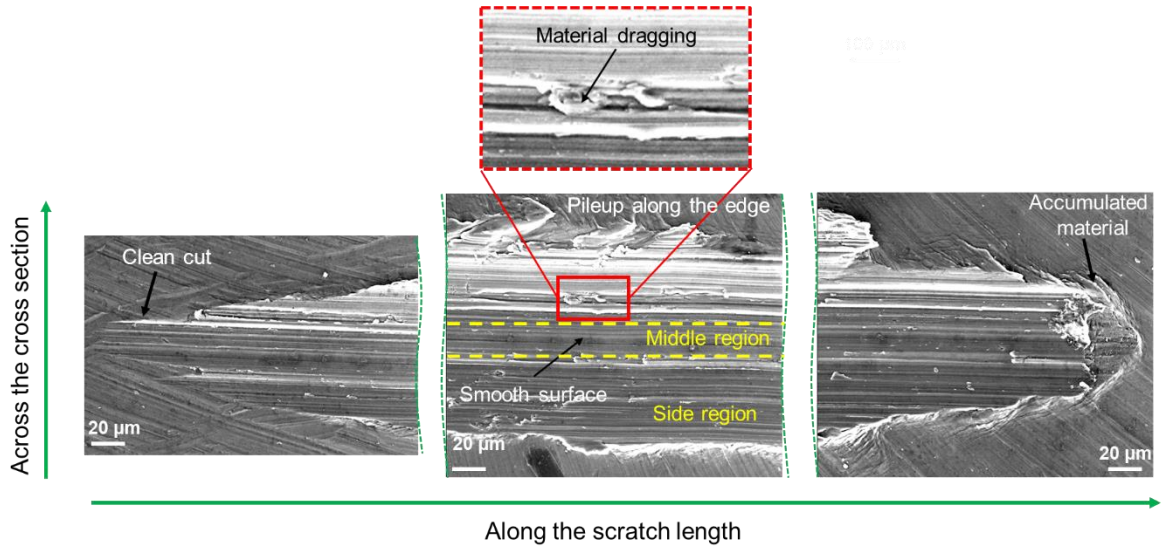

Figure 18. Analysis of the single scratch micrograph showing different features of the scratch including material pile-up and accumulated materials at cutting speed of $v_c = 80$ mm/min

Sub-surface deformation is inevitable during a contact mode cutting process including scratching. Figure 19(a) shows an enlarged image of an edge of the groove along with wrinkles on the parent material surface. The deformed zone containing wrinkled material layers are quantitatively defined in terms of 'deformation length (l_{def})'. The deformed or wrinkled material makes an angle with the undeformed material vector, termed as 'deformation angle (θ_{def})'. The deformation angle variation with respect to the cutting speed is plotted in Figure 19(b). The material layers affected by the scratch align in the direction of the cutting velocity vector. The higher the velocity, the stronger is the alignment of the material layers. Accordingly, the deformation angle is higher at high cutting speeds. However, the results presented in Figure 16 indicate an opposite trend. The deformation angle reduces with an increase in the cutting speed. This phenomenon is attributed to the lower stress build up and high elastic recovery of the material at higher cutting speeds. The material undergoes more drag at high cutting speed thereby reversing the deformation and lowering the deformation angle. The deformation zone length, l_{def} variation with respect to cutting speed is also plotted in Figure 19(b). The deformation length increases with increasing cutting speed to approximately 60 µm at the cutting speed of 20 mm/min, and 73 µm at 160 mm/min.

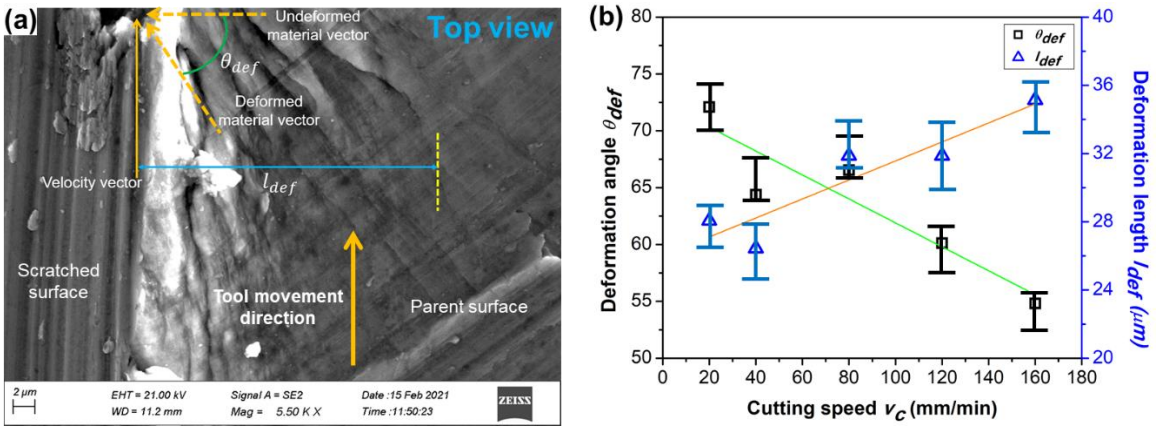

Figure 19. (a) Material deformation in the sub-surface of the scratch at cutting speed $v_c = 80$ mm/min and (b) deformation angle and deformation zone length with respect to cutting speed

3.2 Material removal mechanism during subsequent scratching

In this section, the mechanism of two consecutively made scratches separated by a certain distance is discussed. Scratching force for the first scratch was found to be same as single scratch but the force for the second scratch was found to vary depending on the spacing between the scratches. The force profiles for the second scratch are presented in Figures 20(a) to (d) with increasing separation distance. It was observed that the maximum force increases as the separation distance between the adjacent scratches changes from 20 µm to 120 µm. When the separation distance is low i.e., 20 µm, the second scratch mostly overlaps with the first scratch, and the amount of material removed during the second scratch is very low. This results in lesser resistance to scratching leading to the reduction of forces. As the interspacing increases, more material is to be removed during the second scratch leads to increased forces. Another perspective to explain this mechanism can be the fact that during a scratch, a dislocation forest is emitted which spreads along and to the side of scratches. An adjacent cut made in the area engulfed by this forest of dislocations will have pre-existing plasticity transporting dislocations which eases the removal and hence leading to lower forces. Conversely, a scratch far from the area affected by dislocations will need these dislocations to be introduced freshly into the

workpiece which will need more specific work and hence the reason for higher forces which are comparable to a standalone single scratch.

The maximum normal and cutting forces during singular and subsequent scratches are plotted in Figure 20(e). It is evident that forces during the second scratch reach to the level of the first scratch, for the spacing between scratches of 160 µm.

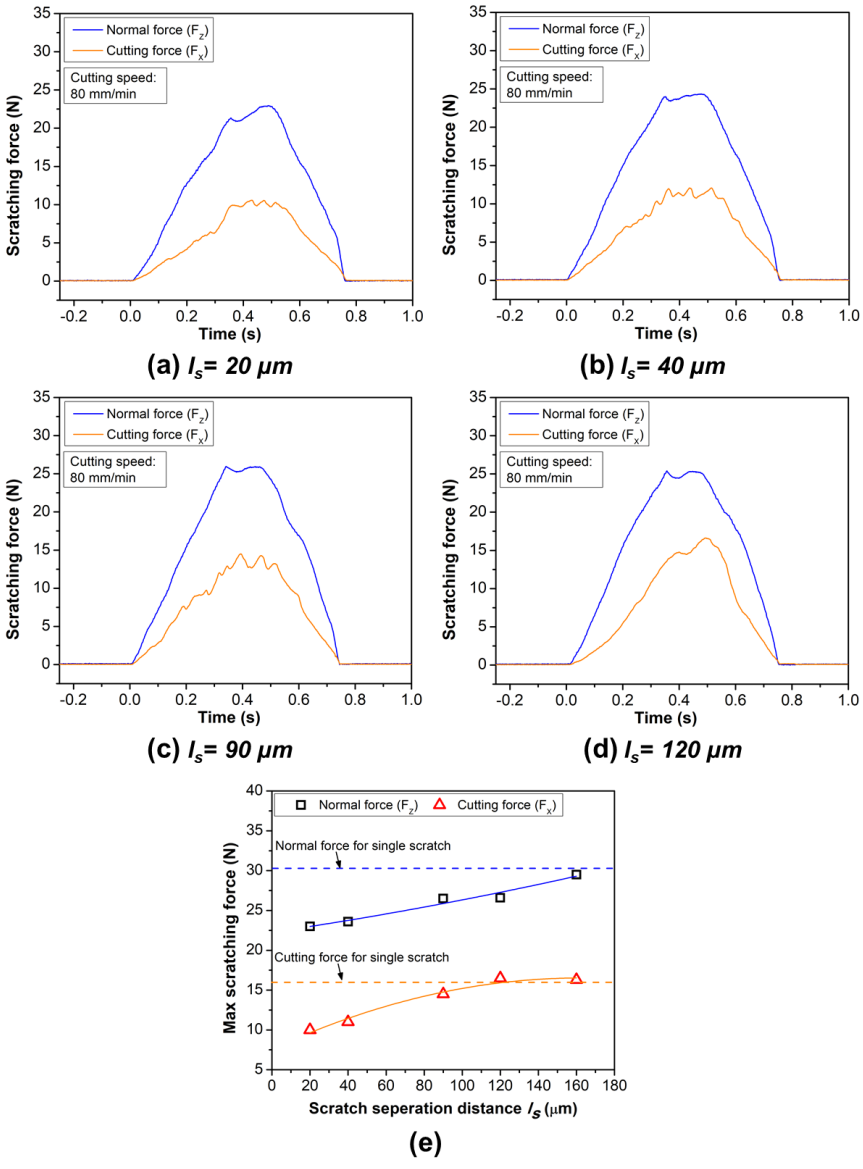

Figure 20. (a)-(d) Scratch force profiles for different spacings of the two scratches and (e) comparison of forces for single scratch and sequential scratches

The microscopic images of scratches with different separation distances (l_s) are presented in Figure 21. A mid-section cut showing 3D profile of the scratches, at separation distances of 40

μm and 90 μm is shown in Figure 22(a), along with the material pile-up mechanism compared in both cases in Figure 22(b). It was observed that the cross section of the groove appears to be almost semi-circular in case of low l_s value of 40 μm, whereas the groove cross section appears to be a distorted semi-circle having a mid-path ridge feature for l_s value of 90 μm. Further, it was seen that when the second scratch follows the first scratch at small l_s, the tool tip removes almost all the material leaving insignificant material at the toe. As l_s increases, the material below the intersection of the circular cross sections of the successive tool paths remains attached to the work surface in a highly strained condition. These features contribute to the surface roughness parameters and poor surface quality during machining [40]. Therefore, in general, it can be said that an optimal grit spacing of 0.3R will lead to avoiding coarser defects, such as microchipping of grooves and ridges. In the current study, for the tool radius of R=120 μm and l_s= 40 μm, intra-scratch feature or ridge were not observed. During grinding, a number of grits interacts with the workpiece simultaneously, and the grit spacing on a grinding wheel significantly affects the surface generation. In case where the grit spacing is too small, severe ploughing will be evident due to material side flow from the grit surfaces. If the grit spacing is too large, a large amount of inter-grit material will be left out leading to poor surface generation. Therefore, the appropriate grit spacing on a monolayer brazed grinding wheel is essential and can be selected based on the above findings.

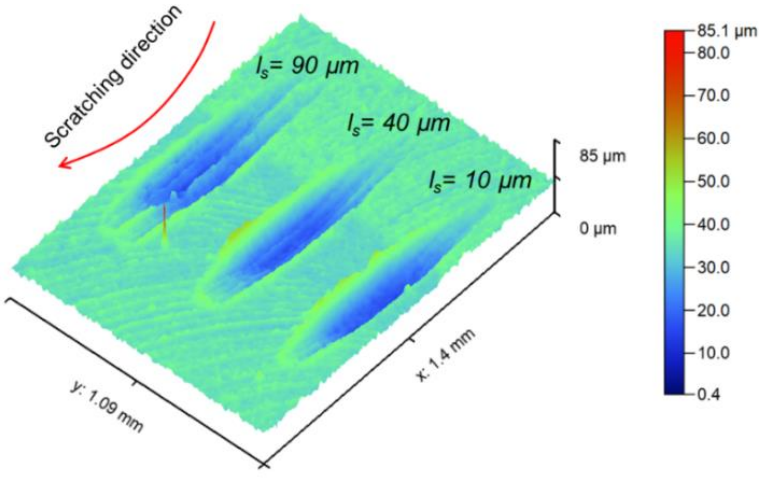

Figure 21. Two consecutive scratches formed at different separation distances, at cutting speed v_c = 80 mm/min and scratch slope 4/50

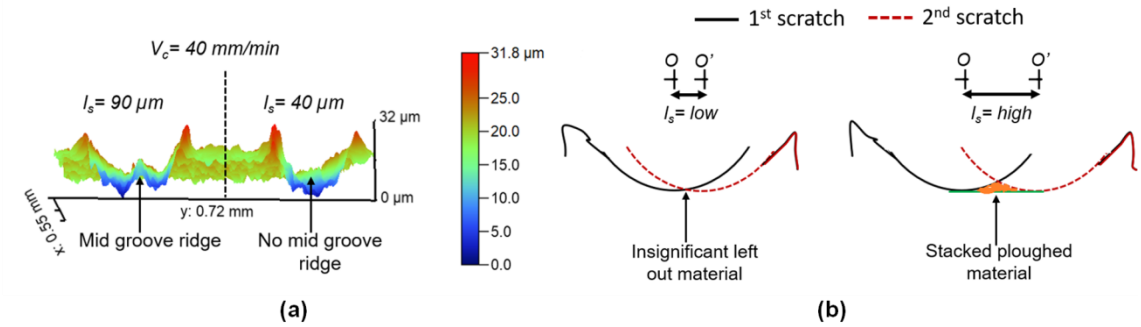

Figure 22. (a) Mid-section profile of scratches and (b) Material removal mechanism and inter-groove feature formation mechanism during subsequent scratching at different interspacings

The pile-up ratio with respect to the separation distance l_s is plotted in Figure 23(a). The ratio reduces as l_s increases. However, the pile-up ratio was observed to be increasing when the l_s increases beyond 120 µm. At low separation distance, pile-up was more at the outer edge of the second scratch. This was due to material imbalance in front of the grit. As l_s increases, the material balance in front of the grit during second scratch increases and the ploughing reduces.

The material removal area, as defined in Figure 6, with respect to the separation distance is plotted in Figure 23(b). When the separation distance between successive scratches is small, the toolpath becomes overlapped and therefore the net material removal area is very small. As l_s increases, the material removal during second scratch increases. At a position, where two groove cross-sections are on the verge of separation or separate by a minimal distance, the material removal becomes maximum. This is because of the addition of material removed from two grooves and the thin layer of the inter-groove material that is removed due to its very low resistance.

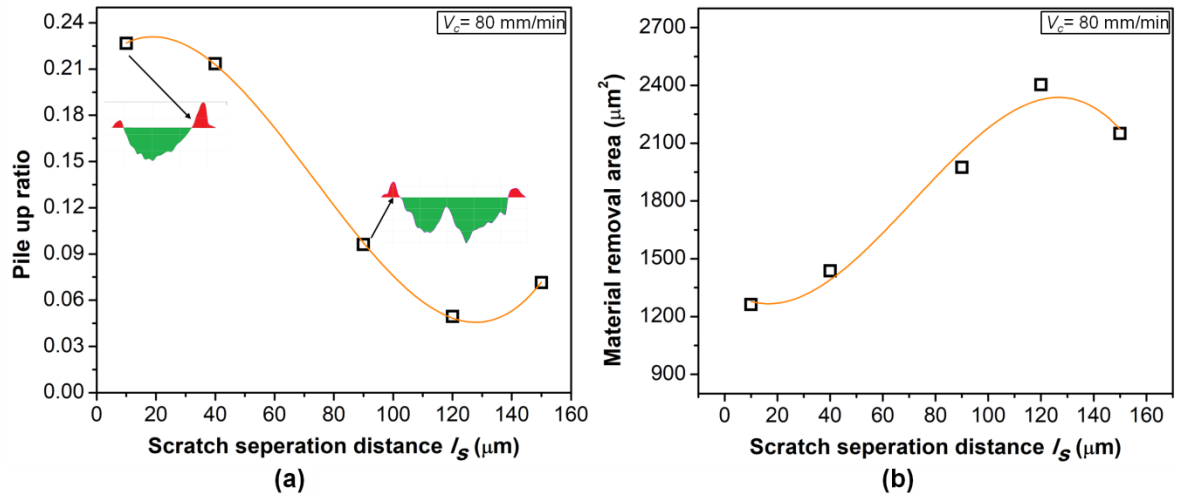

Figure 23. (a) Pile-up ratio and material removal area (MRA) variation with scratch separation distance

3.3 Effect of tool wear on scratch morphology

Diamond grit undergoes an abrasive wear with an increase in the cutting length or machining time. Profile of indenter tip after machining 50 and 80 passes is shown in Figure 24(a) and 24(b), respectively. Tip radius of the indenter increases from 119 μm to around 131.6 μm in the abrasive wear stage. As the tip gets rounded, the pile-up increases and the minimum chip thickness moves to higher side. In case of fracture of the tip, multiple tip are formed and the obtained scratch profile looks similar to the double scratch profile. Effective grit engaging radius for a fractured tip is plotted in Figure 25. It is evident that the effective engaging radius reduces as the depth of cut increases. At lower depth of cut, material was not effectively lifted upwards rather the material flowed sideways which led to a large grit engaging radius. Therefore, it is advisable to use larger depths of cut with a fractured tip for effective material removal, however, process forces will be higher.

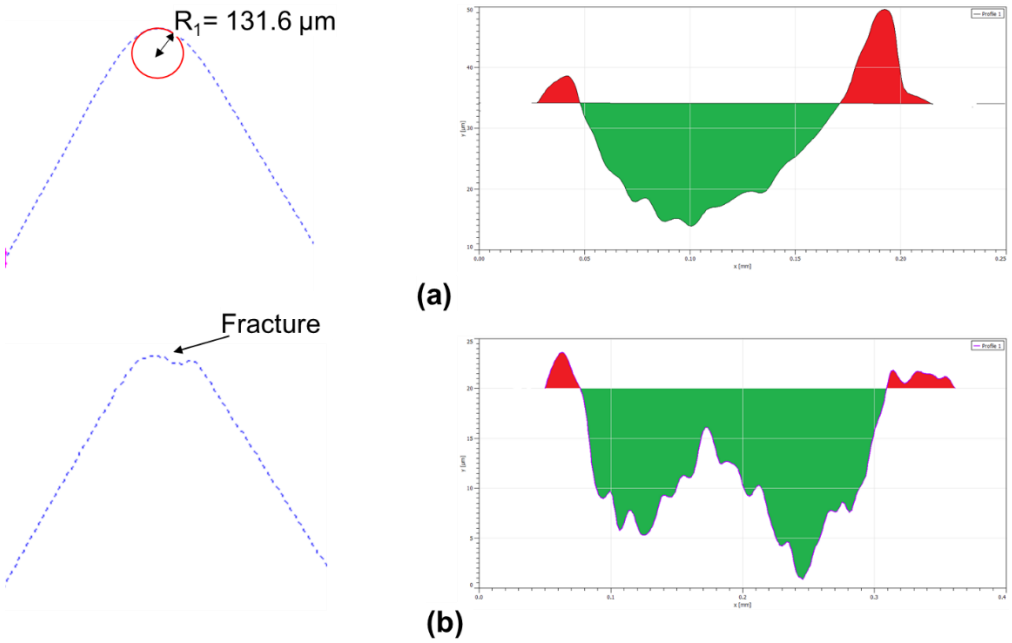

Figure 24. Tool tip profile and corresponding scratch profile (a) for edge rounding type wear, (b) edge fracture wear

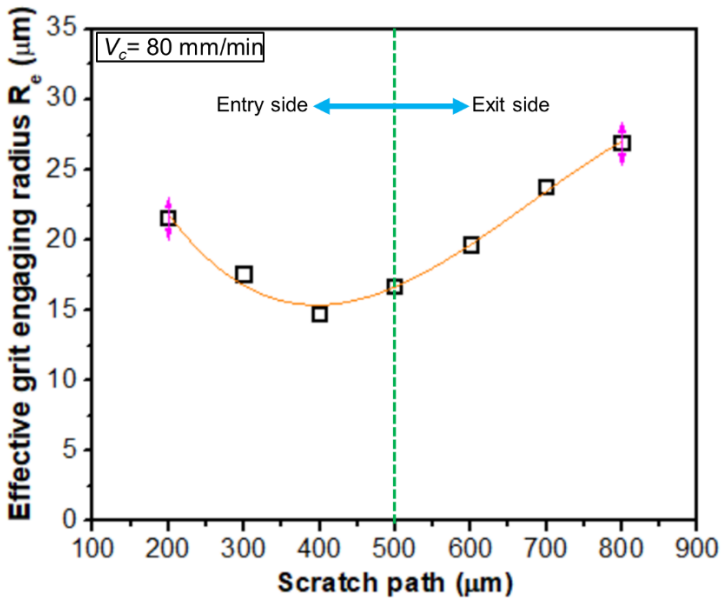

Figure 25. Variation of effective grit engaging radius along the scratch path for a fractured edge tool tip

Conclusions

This study focuses on investigating the material removal mechanism during scratching by means of multiple scratching experiments comparing the influence of the spacing between two subsequent scratches. A semi-empirical analytical force model was developed to compare and contrast the mode of material removal. New insights were obtained in terms of the material pile

up ratio, coarse defects such as ridges and microdebris, and mode of material removal such as ploughing, rubbing and plastic flow as summarised below:

- During single grit scratching, axial cutting forces remained almost one third of the normal (thrust) forces. A larger tip radius of the grit produces severe ploughing and a dead metal zone which results in increasing normal forces. The forces showed an inverse relation with cutting speed.
- Amount of pile-up was large at the beginning of the scratch, it reduces in the middle of the scratch where cutting depth is maximum, and again increases at the exit side of the scratch due to work material accumulation in front of the grit.
- Cutting speed shows a profound effect on minimum chip thickness during cutting of Ti-6Al-4V using a large radius tool. At low cutting speed, diffusion constant and immobile defects could be high due to low temperatures in the cutting zone. This could lead to hindered shearing and dominant ploughing on the material surface which could result in a higher minimum chip thickness. As the cutting speed and in turn the temperature increase, immobile defect counts get reduced and dislocations could jump out of the intrinsic plane which could lead to proper shearing and reduced minimum chip thickness value.
- An analytical model of ploughing and flow induced forces shows that the contribution of ploughing forces is more at low chip thickness values and forces in flow regime become dominant when chip thickness increases. The experiments show that the minimum chip thickness lies between 0.1 to 0.2 times the edge radius of the tool. It was also varified using the analytical model proposed here.
- Elastic recovery scales linearly with the cutting speed. The amount of elastic recovery varies being maximum at middle of the scratch to minimum towards the free surface.

Finite element simulations show the stress-strain relationship at different nodes across the cross section which justifies the variation in elastic recovery amount.

- The separation distance between the two consecutive scratches affects the scratching process. A lower pitch between the two scratches was shown to require less forces to make a scratch and beyond a certain threshold pitch, the forces become comparable to the isolated single scratch. Also, a lower separation distance results in a larger pile-up forming an intact semi-circular cross-sectional groove. As the separation distance increases, a mid-groove ridge gets formed. To prevent the ridge formation, an optimal spacing between the scratches was established to be about one-third of the grit radius.

Acknowledgements

SG greatly acknowledge the financial support provided by the UKRI via Grants No. EP/L016567/1, EP/S013652/1, EP/S036180/1, EP/T001100/1 and EP/T024607/1, Transforming the Foundation Industries NetworkPlus Feasibility study award to LSBU (EP/V026402/1), Royal Academy of Engineering via Grants No. IAPP18-19\295 and TSP1332, EURAMET EMPIR A185 (2018), EU Cost Actions (CA15102, CA18125, CA18224 and CA16235), The Hubert Curien Partnership award 2022 from the British Council and Newton Fellowship award from the Royal Society (NIF\R1\191571). Wherever applicable, the work made use of Isambard Bristol, UK supercomputing service accessed by Resource Allocation Panel (RAP) grant as well as ARCHER2 resources (Project e648).

References:

1. Tian L, Fu Y, Xu J, et al (2015) The influence of speed on material removal mechanism in high speed grinding with single grit. Int J Mach Tools Manuf 89:192–201. https://doi.org/10.1016/j.ijmachtools.2014.11.010

2. Huang N, Yan Y, Zhou P, et al (2020) Elastic recovery of monocrystalline silicon during

ultra-fine rotational grinding. Precis Eng 65:64–71. https://doi.org/10.1016/j.precisioneng.2020.05.004

3. Kovalchenko AM, Goel S, Zakiev IM, et al (2019) Suppressing scratch-induced brittle fracture in silicon by geometric design modification of the abrasive grits. J Mater Res Technol 8:703–712. https://doi.org/10.1016/j.jmrt.2018.05.016

4. Matsuo T, Toyoura S, Oshima E, Ohbuchi Y (1989) Effect of Grain Shape on Cutting Force in Superabrasive Single-Grit Tests. CIRP Ann - Manuf Technol 38:323–326. https://doi.org/10.1016/S0007-8506(07)62714-0

5. Ohbuchi Y, Matsuo T (1991) Force and Chip Formation in Single-Grit Orthogonal Cutting with Shaped CBN and Diamond Grains. CIRP Ann - Manuf Technol 40:327–330. https://doi.org/10.1016/S0007-8506(07)61998-2

6. Wang H, Subhash G, Chandra A (2001) Characteristics of single-grit rotating scratch with a conical tool on pure titanium. Wear 249:566–581. https://doi.org/10.1016/S0043-1648(01)00585-3

7. Subhash G, Loukus JE, Pandit SM (2002) Application of data dependent systems approach for evaluation of fracture modes during a single-grit scratching. Mech Mater 34:25–42. https://doi.org/10.1016/S0167-6636(01)00083-7

8. Chena X, Öpözb TT (2010) Simulation of grinding surface creation - A single grit approach. Adv Mater Res 126–128:23–28. https://doi.org/10.4028/www.scientific.net/AMR.126-128.23

9. Chen X, Opoz TT, Oluwajobi A (2017) Analysis of grinding surface creation by single-grit approach. J Manuf Sci Eng Trans ASME 139:. https://doi.org/10.1115/1.4037992

10. Singh V, Ghosh S, Rao PV (2011) Comparative study of specific ploughing energy for

mild steel and composite ceramics using single grit scratch tests. Mater Manuf Process 26:272–281. https://doi.org/10.1080/10426914.2010.526979

11. Öpöz TT, Chen X (2012) Experimental investigation of material removal mechanism in single grit grinding. Int J Mach Tools Manuf 63:32–40. https://doi.org/10.1016/j.ijmachtools.2012.07.010

12. Ghosh S, Chattopadhyay AB, Paul S (2010) Study of grinding mechanics by single grit grinding test. Int J Precis Technol 1:356. https://doi.org/10.1504/ijptech.2010.031663

13. Chen Z, Tian L, Fu Y, et al (2012) Chip formation of nickel-based superalloy in high speed grinding with single diamond grit. Int J Abras Technol 5:93–106. https://doi.org/10.1504/IJAT.2012.048537

14. Gao C, Liu M (2019) Effects of Normal Load on the Coefficient of Friction by Microscratch Test of Copper with a Spherical Indenter. Tribol Lett 67:1–12. https://doi.org/10.1007/s11249-018-1124-9

15. Gao C, Liu M (2020) Effect of sample tilt on measurement of friction coefficient by constant-load scratch testing of copper with a spherical indenter. J Test Eval 48:970–989. https://doi.org/10.1520/JTE20180719

16. Liu M, Yan F (2021) Comparison of Microscratch Responses of Metals Between Berkovich and Rockwell C Indenters Under Progressive Normal Force. Tribol Lett 69:1–16. https://doi.org/10.1007/s11249-021-01530-x

17. Liu M (2021) Microscratch of copper by a Rockwell C diamond indenter under a constant load. Nanotechnol Precis Eng 4:. https://doi.org/10.1063/10.0005065

18. Axinte D, Butler-Smith P, Akgun C, Kolluru K (2013) On the influence of single grit micro-geometry on grinding behavior of ductile and brittle materials. Int J Mach Tools

Manuf 74:12–18. https://doi.org/10.1016/j.ijmachtools.2013.06.002

19. Wu H, Huang H, Jiang F, Xu X (2016) Mechanical wear of different crystallographic orientations for single abrasive diamond scratching on Ta12W. Int J Refract Met Hard Mater 54:260–269. https://doi.org/10.1016/j.ijrmhm.2015.07.038

20. Wu H (2021) Wear characteristics of single diamond grit scratching on sapphire with different contact forms. Ceram Int 47:8840–8848. https://doi.org/10.1016/j.ceramint.2020.12.005

21. Yiming M, Zhonghua Y, Zhensheng Y (2017) Experimental investigation of correlation between attrition wear and features of acoustic emission signals in single-grit grinding. Int J Adv Manuf Technol 93:2275–2287. https://doi.org/10.1007/s00170-017-0687-1

22. Öpöz TT, Chen X (2015) Experimental study on single grit grinding of Inconel 718. Proc Inst Mech Eng Part B J Eng Manuf 229:713–726. https://doi.org/10.1177/0954405414531114

23. Yiming M, Zhonghua Y, Zhensheng Y (2017) Numerical investigation of the evolution of grit fracture and its impact on cutting performance in single grit grinding. Int J Adv Manuf Technol 89:3271–3284. https://doi.org/10.1007/s00170-016-9249-1

24. Zhu Y, Ding W, Rao Z, Yang C (2019) Micro-fracture mechanism of polycrystalline CBN grain during single grain scratching tests based on fractal dimension analysis. Precis Eng 59:26–36. https://doi.org/10.1016/j.precisioneng.2019.05.010

25. Setti D, Kirsch B, Aurich JC (2019) Experimental investigations and kinematic simulation of single grit scratched surfaces considering pile-up behaviour: grinding perspective. Int J Adv Manuf Technol 103:471–485. https://doi.org/10.1007/s00170-019-03522-7

26. Zhao B, Xiao G, Ding W, et al (2020) Effect of grain contents of a single-aggregated cubic boron nitride grain on material removal mechanism during Ti–6Al–4V alloy grinding. Ceram Int 46:17666–17674. https://doi.org/10.1016/j.ceramint.2020.04.069

27. Zhao J, Liu Z (2020) Plastic flow behavior for machined surface material Ti-6Al-4V with rotary ultrasonic burnishing. J Mater Res Technol 9:2387–2401. https://doi.org/10.1016/j.jmrt.2019.12.071

28. Wang Y, Zou B, Wang J, et al (2020) Effect of the progressive tool wear on surface topography and chip formation in micro-milling of Ti–6Al–4V using Ti(C7N3)-based cermet micro-mill. Tribol Int 141:105900. https://doi.org/10.1016/j.triboint.2019.105900

29. Chen G, Ge J, Lu L, et al (2021) Mechanism of ultra-high-speed cutting of Ti-6Al-4V alloy considering time-dependent microstructure and mechanical behaviors. Int J Adv Manuf Technol 113:193–213. https://doi.org/10.1007/s00170-021-06589-3

30. Pratap A, Patra K (2020) Evolution of chemo-mechanical effects during single grit diamond scratching of monocrystalline silicon in the presence of potassium hydroxide. Wear 452–453:203292

31. Bai J, Bai Q, Tong Z, Chen G (2018) The influence of cutting parameters on the defect structure of subsurface in orthogonal cutting of titanium alloy. J Mater Res 33:720–732. https://doi.org/10.1557/jmr.2017.397

32. Park HW, Liang SY (2008) Force modeling of micro-grinding incorporating crystallographic effects. Int J Mach Tools Manuf 48:1658–1667. https://doi.org/10.1016/j.ijmachtools.2008.07.004

33. Pan Y, Zhou P, Yan Y, et al (2021) New insights into the methods for predicting ground

surface roughness in the age of digitalisation. Precis Eng 67:393–418. https://doi.org/10.1016/j.precisioneng.2020.11.001

34. Cheng J, Gong YD (2014) Experimental study of surface generation and force modeling in micro-grinding of single crystal silicon considering crystallographic effects. Int J Mach Tools Manuf 77:1–15. https://doi.org/10.1016/j.ijmachtools.2013.10.003

35. H.W. Park, S. Y. Liang RC (2007) Microgrinding force predictive modelling based on microscale single grain interaction analysis. Int J Manuf Technol Manag 12:25–38. https://doi.org/10.1504/IJMTM.2007.014141

36. Zhang F, Meng B, Geng Y, et al (2016) Friction behavior in nanoscratching of reaction bonded silicon carbide ceramic with Berkovich and sphere indenters. Tribiology Int 97:21–30. https://doi.org/10.1016/j.triboint.2016.01.013

37. Schaal N, Kuster F, Wegener K (2015) Springback in metal cutting with high cutting speeds. Procedia CIRP 31:24–28. https://doi.org/10.1016/j.procir.2015.03.065

38. Liu C, Goel S, Llavori I, et al (2019) Benchmarking of several material constitutive models for tribology, wear, and other mechanical deformation simulations of Ti6Al4V. J Mech Behav Biomed Mater 97:126–137. https://doi.org/10.1016/j.jmbbm.2019.05.013

39. Zhang L, Zhang T, Guo B, et al (2018) Research on the single grit scratching process of oxygen-free copper (OFC). Materials (Basel) 11:1–15. https://doi.org/10.3390/ma11050676

40. Rashid W Bin, Goel S (2016) Advances in the surface defect machining (SDM) of hard steels. J Manuf Process 23:37–46. https://doi.org/10.1016/j.jmapro.2016.05.007

Declaration of interests

☒ The authors declare that they have no known competing financial interests or personal relationships that could have appeared to influence the work reported in this paper.

☐The authors declare the following financial interests/personal relationships which may be considered as potential competing interests:
